Implementation of orographic-drag anisotropy in all flow directions in the Earth System Model CAS-ESM 2.0

Jinbo Xie[1], Minghua Zhang[2,3], Qingcun Zeng[2,4], Zhenghui Xie[1,4], Hailong Liu[1,4], Zhaoyang Chai[2,4], JuanXiong He[2], He Zhang[2]

[1]State Key Laboratory of Numerical Modeling for Atmospheric Sciences and Geophysical Fluid Dynamics, Institute of Atmospheric Physics, Chinese Academy of Sciences, Beijing 100029, China

[2]International Center for Climate and Environment Sciences, Institute of Atmospheric Physics, Chinese Academy of Sciences, Beijing, China

[3]School of Marine and Atmospheric Sciences, State University of New York at Stony Brook, NY, USA

[4]College of Earth and Planetary Sciences, University of Chinese Academy of Sciences, Beijing 100049, China

Submitted to Journal of Advances in Modeling Earth Systems (JAMES)

*Corresponding author: Zhenghui Xie (zxie@lasg.iap.ac.cn)

Key Points:

- A new orographic drag scheme considering anisotropy in all directions for weather and climate models was implemented into the CAS-ESM 2.0.
- The updated CAS-ESM model considered the effects of orographic-drag anisotropy on the global mountain climate.
- The mountain wind and temperature biases from the CAS-ESM simulations were alleviated with the new orographic drag scheme.

Abstract

A reasonable representation of orographic anisotropy in earth system models is vital for improving weather and climate modeling. In this study, we implemented the orographic drag scheme, including 3-D orographic anisotropy (3D-AFD), into the Chinese Academy of Sciences Earth System Model version 2 (CAS-ESM 2.0). Three groups of simulations named sensitivity run, medium-range forecast, and seasonal forecast respectively were conducted using the updated CAS-ESM model together with the original 2-D isotropic scheme (2-D) and the 3-D orographic anisotropy for the eight-direction scheme (3D-8x) to validate its performance. Sensitivity runs indicated that the simulated drag using the original 2-D scheme did not change with the wind directions, while the simulated drag using the updated 3D-AFD showed a smoother transition than that using 3D-8x. The 3D-AFD and 3D-8x had also about 80% larger drag and smaller wind speed of 1m/s than that of the 2-D scheme. Enhanced drag in the medium range and seasonal forecast using the updated CAS-ESM both alleviated the bias of the overestimated wind speed and the cold bias over mountain regions in the 2-D scheme. This was more apparent in winter (0.4-0.5 m/s and ~1K) than that in summer (0.1 m/s and ~0.1K) for the northern hemisphere region, such as the Tibetan Plateau. The vertical wind profile was also improved in the seasonal forecast. The results suggested that a reasonable representation of the orographic anisotropy was important in climate modeling, and the updated model of CAS-ESM with 3D-AFD alleviated the bias of the mountain wind.

Plain Language Summary

The effect of orographic anisotropy is essential for numerical weather prediction in complex terrains. In this study, we implemented an orographic drag scheme considering orographic anisotropy in all flow directions into the global climate model. The aim was to examine the effect of orographic anisotropy on the global mountain climate. It was shown that the new scheme had a smooth transition of the surface drag as a function of wind direction and enhanced drag. This led to the alleviation of the wind bias compared to the original 2-D drag scheme in the global mountain region. This demonstrated that the more explicit representation of the orographic anisotropy for all flow directions was important in climate modeling. Hence, it should be considered more explicitly in climate simulation.

1. Introduction

Understanding the air flow around high mountain ridges and the impact of drag on the air flow are of considerable importance for predicting the dispersion of pollutants, the occurrence of atmospheric turbulence, and for weather forecasting in mountainous regions. The mountain ridges can affect the mountain region's weather and climate in various ways, and one important aspect is the orographic anisotropy. The orographic anisotropy is referred to as the property of being directionally dependent on the sub-grid orography. In general, the orography that generates mountain waves is not isotropic. This means that in the case of the different wind directions, the orography will have different lengths and shapes in the cross-wind and along-wind direction and thus, in the resultant mountain drag. Studies have shown that this drag is substantially more non-linear and high for incoming wind perpendicular to the major axis of an axisymmetric mountain than the flow parallel to that axis [*Epifanio and Durran*, 2001; *Bauer et al.*, 2000; *Wells et al.*, 2008]. Incorporation of this 3-D orographic anisotropy effect in the sub-grid orographic is often neglected [*Gregory et al.*, 1998; *Lott & Miller*, 1997; *Nappo & Chimonas*, 1992]. This may cause a large difference in the amplitude of the orographic drag and the associated meteorological variables, including wind, temperature, and the orographic precipitation that is highly sensitive to the inflow wind direction and the associated drag [*Nuss & Miller*, 2001; *Neiman et al.*, 2011; *Hughes et al.*, 2014; *Picard & Mass*, 2017]. Thus, it is important to incorporate this effect in climate system modeling.

Two types of schemes exist depending on the treatment of orographic specification existing among those that incorporate the orographic anisotropy. The first type derives the orographic drag with the assumption that the orography has an elliptical shape with an

analytical function. In this regard, several parameters have to be determined. The relevant anisotropic parameters in the flow direction are derived using the “best fit” analytical function (fitted against the sub-grid orographic height data) to derive the orographic drag in this direction [*Baines & Palmer*, 1990; *Lott & Miller*, 1997; *Phillips*, 1984; *Scinocca and McFarlane*, 2000]. This treatment, however, hinders the input of a higher-order detail of the terrain shape because it inherently assumes a symmetric terrain shape on the windward and leeward side of the mountain in the inflow direction. The second type, however, avoids the requirement for an a priori assumption of the terrain shape by deriving the anisotropic parameters in a bulk form [*Kim & Doyle*, 2005; *Hong et al.*, 2008; *Choi & Hong*, 2015]. This treatment allows more flexibility by enabling the inclusion of the higher-order moments of the terrain shape for the inflow direction that is shown to be related to the non-linear enhancement of the orographic drag-orographic asymmetry. For example, it is shown to be largely associated with the low-level wave breaking and non-hydrostatic wave trapping in downstream of the orograph [*Kim & Doyle*, 2005; *Hong et al.*, 2008; *Choi & Hong*, 2015]. However, because the derivation for orographic parameters is not so easy and straightforward for angles other than the eight representative directions (e.g., ±0°, ±45°, ±90°, ±135°; see for example, Figures 2 and 6 in *Kim & Doyle*, 2005), this line of treatment is restricted only to these eight representative directions. This consequently may induce sudden jumps in the values of the orographic statistics with small changes in the wind direction and may introduce bias in weather and climate prediction [*Kim and Doyle*, 2005]. To remedy this problem, *Xie et al.* (2020) recently developed a new scheme that allowed the derivation of the parameters for all flow directions. This scheme revised the original parameter derivation method of *Kim & Doyl* (2005) to form a scheme that considers the orographic anisotropy in the derivation of the orographic drag for all flow directions.

In this study, we implemented this orographic drag scheme from *Xie et al.* (2020) into the second version of the Chinese Academy of Sciences Earth System Model (CAS-ESM 2.0) by considering orographic anisotropy for all flow directions. The effect of this 3-D drag scheme with orographic anisotropy for eight directions (3D-8x) and for all flow directions (3D-AFD) on global climate was compared with that of the original 2-D scheme. The paper is organized as follows: section two describes the experiment and design. Section three presents the comparison results for the three groups of simulations, including the sensitivity run, medium-range forecast, and seasonal forecast. Ultimately, the summary and conclusion are provided in section 4.

2. Model development and Experiment Design

In this section, we introduced the new orographic anisotropy scheme for all flow directions and its coupling with the CAS-ESM 2.0. The experiment design was also introduced to compare the updated model with the original 2-D isotropic gravity wave drag scheme.

2.1 Orographic anisotropy scheme for all flow directions (AFD scheme)

The scheme that we implemented in the model was the orographic anisotropy scheme for all flow directions from *Xie et al.* (2020). This scheme was based on the subgrid orographic parameterization from *Kim and Arakawa* (1995) that included the gravity wave drag effect and the drag due to low-level wave breaking and non-hydrostatic wave trapping. The gravity wave stress (τ) at the reference level (h_{ref}) is defined as follows:

$$\tau_{\mathrm{GWD}}=\rho_0 E\frac{m}{\lambda_{eff}}G\frac{|U_0|^3}{N_0}, \quad (1)$$

where

$$\begin{cases} \mathrm{E} = (OA_\theta + 2)^{C_E Fr_0/Fr_c}, \\ \mathrm{m} = (1 + OL_\theta)^{OA_\theta + 1}, \\ \mathrm{G} = \frac{Fr_0^2}{Fr_0^2 + C_G OC^{-1}}, \end{cases} \quad (2)$$

Subscript θ denotes the direction related parameter in the low-level wind direction, and subscript *o* indicates the low-level average between the surface and the reference level h_{ref}. Following *Koo et al.* (2018), the reference level h_{ref} is determined by max ($2\sigma_h$,h_{pbl}) (h_{pbl} is the planetary boundary layer height). ρ_0 is the low-level density; E is the enhancement factor, and it is controlled by OA that represents the shape and location of the sub-grid scale orography relative to the grid; m is the number of sub-grid scale orography; λ_{eff} is the model effective grid length; G is an asymptotic function that provides a smooth transition between the blocking and nonblocking cases; The effect of mountain sharpness is included in G through orographic convexity (OC=$(1/N_B\sigma_h^4)\sum_{j=1}^{N_B}(h_j - \overline{h})^4$, where $\overline{h}$ signifies the average of the coarse grid and sub-grid topography). The orographic convexity represents the sharpness of the mountain and corresponds to the vertical orographic aspect ratio; U_0 is the horizontal wind speed, and N_0 is the Brunt-Vaisala frequency; The coefficients C_E and C_G are set to be 0.8 and 0.5, respectively. Fr_0=$OD*N_0 h_{ref}/U_0$, where OD is the ratio of the crosswind effective orographic length (OLP) and the along-wind OL (e.g. OD=OLP_θ/OL_θ). The vertical stress profile above the reference level is determined according to the linear instability theory [*Lindzen*, 1981] and the nonlinear resonant LLWB adjusted according to the Scorer parameter [*Kim and Arakawa*,1995; *Kim and Doyle*, 2005; *Xie et al.*, 2020]. Further details can be found in *Xie et al.* (2020).

The flow-blokcing drag is also included in the scheme which is estimated as follows:

$$\tau_{FBD}=\frac{1}{2}\rho_0\frac{m}{\Delta_x^2}C_d\Delta_x^p OLP_\theta h_B|U_0|^2, \quad (3)$$

where C_d is the bulk drag coefficient defined by C_d =max{2-1/OD,0}, h_B is the height of the blocked layer, Δ_x^2 is the grid-box area, and Δ_x^p is the grid length in the crosswind direction.

Inclusion of the orographic anisotropy in the scheme is through the derivation of the direction related orographic parameters including effective orographic length (OL), OL in the perpendicular direction of the low-level wind (OLP), orographic asymmetry (OA), and orographic direction (OD). In Xie et al. (2020), derivation of the orographic parameters was revised to enable derivability for all flow directions. In this study, schemes with orographic parameters derived for eight representative directions (3D-8x) and all flow directions (3D-AFD) were utilized for comparison with the original 2-D scheme in CAS-ESM.

2.2 Incorporating the AFD scheme into CAS-ESM 2.0

CAS-ESM is a global earth system model consisting of atmosphere, land, ocean, sea ice model, and additional components of atmospheric aerosol and chemistry, dynamic vegetation, fire, land and ocean biogeochemistry (Zhang et al., 2013; Zhang et al., 2020; Dai et al., 2003; Ji et al., 2013; Zeng et al., 2008; Zeng, 2010; Holland et al., 2012; Liu et al., 2012; Chen et al.,2015; Wei et al.,2019). The atmospheric component of CAS-ESM 2.0 is the fifth version of the Institute of Atmospheric Physics-Atmospheric General Climate Model (IAP-AGCM 5.0) which is a global grid-point model using a finite-difference scheme with a terrain-following σ coordinate. Several novel features of the dynamic core include subtraction of the standard atmospheric stratification, IAP transform, nonlinear iterative time integration and time splitting method, and an adaptive leap-format difference scheme to achieve high parallel efficiency based on 3D

decomposition (Zheng at el., 2013; Zhang et al., 2020; Cao et al., 2020). Various improvements of the parameterizations in IAP-AGCM 5.0 include the atmospheric convection, turbulence, cloud macrophysical and microphysical process, and radiation (further details can be found in Zhang et al., 2020). The original orographic drag scheme in the previous versions of the IAP-AGCM was the 2-D isotropic orographic drag scheme from McFarlane (1987). In this study, The new 3D schemes were implemented into IAP-AGCM 5.0 as a module that had its own input and output: the orographic parameters inputs were sent into the scheme, and the calculated outputs were sent to the IAP-AGCM 5.0. Through the coupling of the IAP-AGCM 5.0 and CAS-ESM 2.0, the impact of the orographic drag scheme on the climate was achieved (Fig. 1). The inputs into the scheme were the orographic scheme related parameters, such as the standard deviation of the subgrid-orography (SGH), OC, OA, OL, and model grid length, which were calculated from the data set of the GTOPO30 30 arcsec digital elevation model from the United States Geological Survey (USGS; *Gesch and Larson*, 1998). They were defined on an approximately 1 km regular latitude-longitude grids following the method proposed in *Xie et al.* (2020). The orographic drag and vertical distribution of the wind tendency were calculated through the scheme, and the tendency was added into the IAP-AGCM 5.0's momentum equation to capture the effects of the wind and thus, the climate.

2.3 Experiment Design

To compare the effect of the new 3-D schemes (3D-8x and 3D-AFD) and the original 2-D scheme on global climate in IAP-AGCM 5.0 and CAS-ESM 2.0, three sets of runs were performed using these three schemes (3D-8x, 3D-AFD, and 2-D scheme) on the horizontal resolution of 1.4° latitude × 1.4° longitude and 30 vertical levels (with the model top at 2.2 hPa). The three sets of runs were sensitivity run, medium-range forecast, and the seasonal forecast simulation. The main difference between these runs was the

197 simulation time: one time step for the sensitivity run, ten days for the medium-range
198 forecast, and three months for the seasonal forecast. In this way, we could compare the
199 impact of the three schemes on CAS-ESM 2.0 simulation using different time scales. The
200 sensitivity runs with the three schemes were carried out by using identical initial
201 conditions. Also, one-time step duration ensured that the effect of the orographic drag
202 schemes on the model climate did not drift too far from the initial condition. These
203 simulations were run under two types of initial conditions: ideal and real-time initial
204 conditions. The ideal condition, which is globally uniform 10 m/s wind input (from
205 bottom to top) for the same direction, was used to diagnose the global spatial difference
206 pattern between the three schemes with the same wind input direction and magnitude on
207 global grids. The experiments were conducted for 360 members of each of the three
208 schemes for 360 wind directions (i.e., 0-359 degrees). The real condition, which is the
209 atmospheric condition (00 UTC 21 January 2016) taken from ERA-Interim reanalysis
210 [*Dee et al.*, 2011], was employed to see if the difference from ideal condition runs could
211 be retained using real-time condition (where the wind direction was different for the
212 global grids) as initial condition inputs. For the medium-range forecast, thirty-one 10-day
213 weather forecasts were conducted using prescribed sea surface temperature (SST) and sea
214 ice concentration (SIC) and real-time conditions for every 0000 UTC during January and
215 July 2016, respectively. The atmospheric initial conditions were forced by the
216 ERA-interim reanalysis interpolated to the IAP-AGCM grid, while the SST and SIC were
217 taken from the Hadley center SST and SIC data [*Rayner et al.*, 2006]. For the land initial
218 condition, the land-atmospheric model was first run for 5 years and then forced with the
219 ERA-Interim reanalysis for one month up to the forecast date. The seasonal forecasts
220 followed a similar setup to that of the medium-range forecast except that the simulations
221 were run for ten ensemble members initialized at 0000 UTC 1^{st} – 10^{th} of November and

May and were run for 4 months for the boreal winter and summer cases, respectively. December 2015 to February 2016 and June-August 2016 time periods of the seasonal forecast were utilized for the analysis.

3. Simulations

In this section, the impact of the orographic drag scheme on the sensitivity run, medium-range forecast, and seasonal forecast was analyzed. The orographic drag scheme first affected the surface drag and hence, the wind. Thus, we assessed the model variable in terms of the surface drag. The impact on wind and temperature were then discussed.

3.1 Sensitivity run

In this section, the sensitivity run initialized with the ideal initial condition was analyzed to show the difference among the 2-D, 3D-8x, and 3D-AFD under controllable wind input. for this reason, we chose the simulations using the 23-degree wind input. This was because while the drag impact for 2-D was the same for all directions, the 3D-AFD was mostly different from 3D-8x near the middle shifting point of the nearby two representative directions for 3D-8x (e.g., ±22.5°, ±67.5°, ±112.5°, ±157.5°). The reason was that the 3D-AFD scheme was developed based on the 3D-8x scheme. That is, this scheme extended from the 8x directions to all flow directions (for further detail, please refer to Xie et al., 2020). As shown in Figure 2 (a-c), while the 3D-AFD and 3D-8x schemes showed a very similar magnitude (which was expected), the 2-D drag seemed to be of a lower magnitude. This was confirmed by the difference between 3D-AFD and 3D-8x with the 2-D scheme (Fig. 2d-e) where both schemes showed a higher drag over the major mountain regions, including Tibetan Plateau, Chersky Range,

the Rocky Mountains, the Alps, the Andes, Greenland, and Antarctica. The largest difference was in the north and southern edge of the Tibetan Plateau and the Andes, where the difference was mostly over 0.5 N/m^2. The regions with the second-largest difference were in the Chersky and Greenland, where the drag points ranged from 0.3 to 0.5 N/m^2. The Rocky Mountain regions were among those that had the smallest difference, where the range was about 0.1-0.3 N/m^2. Overall, the drags of the 3D-AFD and the 3D-8x scheme were approximately 80% larger than that of the 2-D scheme. As for the difference between 3D-AFD and 3D-8x (Fig. 2f), the pattern was similar to the aforementioned difference between the two 3D-schemes with the 2-D, although the difference was much smaller in magnitude and less extended in size. The drags of the 3D-AFD was overall 20% larger than that of the 3D-8x scheme. In summary, for the representative direction of the 23 degrees, the 3D-AFD predominantly had the largest drag, then the 3D-8x had the second-largest drag, and the 2-D scheme had the smallest drag. Consistent with the drag difference pattern, the bottom level wind speed (defined by the lowest model level of the ideal simulation) for both the 3D schemes was smaller in the global mountain region than that of the 2D scheme (Fig. 3ab). Also, the 3D-AFD was smaller than that of the 3D-8x (Fig. 3c).

To depict a full picture of the drag difference, four points were also chosen to show their difference as a function of the wind direction (Fig. 4). The first point (71.7E, 40.4N) was a point in the western border of the Tibetan Plateau (Fig. 4a). For the 2D scheme, the drag was the same for the whole direction as a result of the isotropic drag. For the 3D schemes, however, they showed a change with the wind direction as expected. The 3D schemes were overall larger than the 2D drag for the southerly wind directions while smaller for the northerly wind directions (Fig. 4a). Between the two 3D schemes, the 3D-AFD had a smoother shift of the drag value than that of the 3D-8x scheme with a

piecewise function. The largest difference occurred near the middle of the two representative directions (e.g., ±22.5°, ±67.5°, ±112.5°, ±157.5°). This was not against our expectation as it was already mentioned and analyzed in Xie et al. (2020). The above conclusion is mainly focused on the point that set the Alaska edge of the Rocky Mountain ranges (167.3E, 63.1N) (Fig. 4c), which have a similar topography orientation than that of the first point. For the points in the Chersky range (167.3E, 63.1N) and the Colorado Rocky mountain range (239.1E, 67.1N), however, the orientation was more symmetric and thus, there were two wind direction intervals where the drag was larger than that of the 2D scheme (Fig. 4b and Fig. 4d). Overall, the 3-D schemes allowed more variables by considering the topographic orientation in the calculation of the surface drag, and the result was chiefly larger than that of the 2-D scheme.

In the above section, we compared the drag impact under the ideal situation. In the following, however, we compare the drag impact under a real situation initialized using the ECMWF data on Jan 21^{st,} 2016 (Fig. 5). In this way, we could find out whether or not the difference observed in the idealized simulations could be retained when using a near-real condition. The real condition in this time showed that the wind speed in the mountain region was near 10 m/s in the northern hemisphere, which was quite typical in the boreal winter (Fig. 5). This resulted in an overall drag (Fig. 6) that had a similar magnitude compared to that of the idealized simulations (Figure 3), except for some regions like the Chersky ranges and the Alps which had a near-zero amplitude because of the less wind in the real condition. For the other regions, the drag results generally resembled those of the idealized simulation (Fig. 6).

The above drag patterns led to an overall similar wind speed difference between the schemes in the near-real simulation compared to that of the idealized simulation for the

3D schemes minus the 2D scheme (Fig. 7a and Fig. 7b). For the difference between the 3D schemes (Fig. 7c), however, the differences were not very clear since the wind in the real condition was not likely to be always in the aforementioned shifting points. Thus, this contributed to a smaller but still clear difference between the 3D-AFD and the 3D-8x scheme. All in all, the simulations that used the real condition as initial value still retained most of the impact of the scheme difference that was apparent in the idealized simulations.

3.2 Medium-range forecast

Besides the sensitivity run, we also evaluated the medium-range forecasts. Figure 8 shows day 5 of the forecast of the 10-m wind speed difference with the observation and the difference between schemes. Both forecasts through January and July initial conditions were compared. Compared to the global ERA-Interim 10-m wind speed in January and July, the IAP-AGCM with the 2-D scheme showed an overall overestimated wind on the continent except for the mountain regions of the west and southern-west border of the Tibetan Plateau and the Chersky ranges (Figs. 8a and 8d). The bias ranged from 0.5-1.5 m/s, with the largest and elongated pattern in the west and southern border of the Tibetan Plateau. This pattern also existed in the July forecast with an overall similar magnitude (Fig. 8d). The 3D-8x and 3D-AFD, however, alleviated this overestimation bias (Figs. 8bc and 8ef). The 3D scheme alleviated the bias by about 0.5 m/s in the January forecast and 0.15-0.3 m/s in the July forecast. The difference was larger in the January forecast as the climatological wind speed was larger in boreal winter for the northern hemisphere, and vice versa for the southern hemisphere. This alleviation was also shown in the January forecast of the Chersky ranges.

Associated with the change of the wind through drag was the change in the surface

317 temperature. It was demonstrated that the 3D schemes alleviated the pan-Tibetan Plateau
318 cold bias in the January forecast (both schemes showed a similar magnitude of about
319 0.5-1K (Fig. 9a)). This alleviation also spanned northern regions up to the Siberian region
320 and the northern part of the Rocky mountain (Fig. 9a). For the July forecast, however, the
321 impact was much smaller, and the bias still existed (Fig. 9d).

322 The overall alleviation of the 10-m wind speed and temperature biases were
323 associated with the enhanced column drag in the mountain regions with the 3D schemes
324 compared to the 2D scheme in both the January and July forecasts (Fig. 10). This was
325 shown in the west and eastern border of the Tibetan Plateau and the Chersky ranges.
326 Enhanced drag in these regions tended to exert a drag on the surface wind, and thus,
327 decelerated the near-surface wind. The enhanced drag likely came from the
328 implementation of the enhanced non-linear drag scheme [Xie et al., 2020] as compared to
329 the original linear drag scheme from McFarlane et al. (1987). This caused a more
330 near-surface drag and hence, decreased surface wind. Overall, the enhanced drag using
331 the 3D-schemes decreased the overestimation bias in the medium-range forecast of the
332 10-m wind speed over most of the mountain regions, including the Tibetan Plateau.

333 ## 3.3 Seasonal forecast

334 The outcome in the medium-range forecast was also apparent in the seasonal
335 simulation (Figs.11), where the overestimated regions were in the western and southern
336 flank of the Tibetan plateau and Chersky ranges (Fig. 11a) with a magnitude of near 0.3
337 m/s. However, the 3-D schemes alleviated this bias (Figs. 11b-c). For the forecast in the
338 summer season (Figs.11e-f), the difference was smaller except for the Andes, where the
339 drag tended to decelerate large wind in the western flank of the Andes (Fig. 11f). These
340 effects were generally associated with the enhanced drag due to the implementation of the

341 drag scheme (Fig. 13). In general, the enhanced drag provided by the 3D-schemes was
342 shown to alleviate the excessive 10-m wind speed in the major mountain regions, such as
343 the Tibetan Plateau, the Rocky Mountains, and the Andes Mountain.

344 The surface temperature was also changed along with the wind change (Fig. 12) in
345 the 3D schemes and the 2D scheme, although differences also existed between the two
346 schemes. In the winter, the 2D scheme forecast generally showed a cold bias in the north
347 polar region spanning to the Tibetan Plateau, along with a minor warm bias in the
348 Chersky ranges (Fig. 12a). Compared to the 2-D scheme forecast, the 3D-8x scheme
349 tended to show a warming that spanned from the Tibetan Plateau up to the Northern
350 Siberian coast with the warming that focused on the Tibetan and Altai Mountain region
351 (Figs. 12b). For the 3D-AFD scheme, the warming tended to focus on the northern region
352 that spanned from the northern Siberian coast to northern Korea. This largely alleviated
353 the original winter cold bias in the northern Siberian coast. In summer, the model forecast
354 tended to show a smaller bias than that of the winter forecast, with a cold bias on the
355 southern border of the Tibetan Plateau and a warm bias on the Altai mountain region (Fig.
356 12d). Both 3D schemes showed a smaller difference compared to the 2-D scheme in
357 winter (Fig. 12ef).

358 In addition to the impact on the near-surface wind, the impact of the 3-D drag scheme
359 was also evident in the vertical profile shown in Fig.14. Simulation with the original 2-D
360 drag scheme indicated an overall change of the zonal wind bias as a function of latitude
361 compared to the ERA-interim data in both winter and summer (Fig. 12a and 12d). For
362 winter, this included a large underestimation near the 60S, 0, and the 40N, while an
363 overestimation in the south pole, 20N, and north of 55N (Fig. 12a). For summer, this
364 included an underestimation in the 60S, 40S, 0, 45N, and north of 80N (Fig. 12d).

In winter, the 3D-8x scheme tended to alleviate the underestimated zonal wind bias around 35N and the overestimated zonal wind bias around 60N (Fig. 12b). The 3D-AFD was similar to that of the 3D-8x scheme except that the alleviation in the northern hemisphere was smaller, while there was an alleviation of the underestimated wind speed in the tropics (Fig. 12c). The southern hemisphere zonal wind change in 3D-AFD was also smaller than that of the 3D-8x scheme. In summer, however, the two 3-D schemes showed an overall similar change compared to that of the 2-D scheme, except for the southern hemisphere, where the 3D-8x scheme alleviated more underestimated zonal wind than that of the 3D-AFD scheme (Figs. 12ef). Overall, the 3D schemes tended to alleviate part of the vertical wind bias in the seasonal forecast simulation as compared to the original 2-D scheme in the CAS-ESM.

4. Discussion and conclusion

In this study, an orographic drag scheme that included orographic anisotropy for all flow direction from Xie et al. (2020) was implemented into the CAS-ESM 2.0 to evaluate the effect of orographic anisotropy on global climate. We conducted three sets of experiments (sensitivity run, medium-range forecast, and seasonal forecast) using the CAS-ESM 2.0 with prescribed SST and SIC data with the three schemes to analyze the effect of the orographic anisotropy on the global climate. The sensitivity experiment using idealized globally uniform 10 m/s wind (from bottom to top) with different wind directions demonstrated that both 3D schemes showed a higher drag than the 2D scheme, both of which were about 80% larger. Also, the 3D-AFD was about 20% of that of the 3D-8x scheme. The drag resulted in an overall lower speed of over 1 m/s in the global mountain regions for the 3D schemes than that of the 2-D scheme, while 3D-AFD was

about 0.5 m/s lower than that of the 3D-8x over the global mountain regions. The sensitivity runs using near-real-time conditions indicated that this difference still existed when the model was initialized with real conditions, especially in the northern high-latitude mountain region (e.g., Chersky ranges and the Alaskan region). Analysis of the medium-range and the seasonal forecast demonstrated that through enhanced drag, the new schemes alleviated the overestimated wind bias in the mountain regions, including the Tibetan Plateau and Chersky ranges. It was shown that the 3-D drag schemes also helped to alleviate the bias in the surface wind and temperature and part of the vertical wind profile as compared to the ERA-Interim data in the seasonal forecast simulations. This included overestimated winter wind and cold bias in the Tibetan Plateau, and the alleviation of the overestimated boreal winter zonal wind in the northern hemisphere and overestimated boreal summer zonal wind in the new 3-D schemes compared to the 2-D scheme forecast. This proved that the orographic drag was important in climate modeling and should be considered more explicitly in climate simulation. Also, the enhanced drag could alleviate the surface wind bias in global climate modeling. The research results have a profound potential for use in future climate simulations. The enhanced drag scheme may help to improve the dynamic aspects of the simulation. The transport of the flow including moist is another aspect that may be affected. Such effects may depend on variables such as snow and precipitation. Studies of the impact of the 3D schemes on the precipitation and snow may deserve future work.

Acknowledgments

This research was supported by Grant 2016YFB0200800 from the National Major Research High Performance Computing Program of China and Grant 41806034 from the

National Science Foundation of China, and the National Key Scientific and Technological Infrastructure project "Earth System Science Numerical Simulator Facility" (EarthLab). Additional support was provided by the Biological and Environmental Research Division in the Office of Sciences of the U.S. Department of Energy (DOE), and by the National Science Foundation of Stony Brook University. We highly appreciate this generous support. We thank Kangjun Chen who helped to find a repository for data storage. The ERA-Interim data can be found at this website: https://apps.ecmwf.int/datasets/. The data used in the figures can be obtained online through the following website: http://data.lasg.ac.cn/xjb/gwd/.

References

Baines, P. G. and Palmer, T. N. (1990). Rationale for a new physically based parametrization of subgrid scale orographic effects. Tech. Memo. 169. European CENTRE for Medium-Range Weather Forecasts.

Bauer MH, Mayr GJ, Vergeiner I, Pichler H. Strongly nonlinear flow over and around a three-dimensional mountain as a function of the horizontal aspect ratio. J Atmos Sci. (2000) 57:3971–3991. doi: 10.1175/1520-0469(2001)058< 3971:SNFOAA> 2.0.CO;2.

Choi, H.-J., & Hong, S.-Y. (2015). An updated subgrid orographic parameterization for global atmospheric forecast models. Journal of Geophysical Research: Atmospheres, 120, 12,445–12,457. https://doi.org/10.1002/2015JD024230

Epifanio CC, Durran DR. Three-dimensional effects in high-drag-state flows over long ridges. J Atmos Sci. (2001) 58:1051–65. doi:10.1175/1520-0469(2001)058<

1051:TDEIHD> 2.0.CO;2

Gesch, D. B. and Larson, K. S.: Techniques for development of global 1-kilometer digital elevation models, in: Pecora Thirteenth Symposium, Am. Soc. Photogrammetry Remote Sens., Soiux Falls, South Dakota, 1998.

Gregory, D., Shutts, G. J., & Mitchell, J. R. (1998). A new gravity-wave-drag scheme incorporating anisotropic orography and low-level wave breaking: Impact upon the climate of the UK Meteorological Office Unified Model. Quarterly Journal of the Royal Meteorological Society, 124, 463–493.

Hong, S.-Y., Choi, J., Chang, E. C., Park, H., & Kim, Y. J. (2008). Lower tropospheric enhancement of gravity wave drag in a global spectral atmospheric forecast model. Weather and Forecasting, 23(3), 523–531. https://doi.org/10.1175/2007WAF2007030.1

Hughes, M., Mahoney, K. M., Neiman, P. J., Moore, B. J., Alexander, M., & Ralph, F. M. (2014). The landfall and inland penetration of a flood-producing atmospheric river in Arizona. Part II: Sensitivity of modeled precipitation to terrain height and atmospheric river orientation. Journal of Hydrometeorology, 15(5), 1954–1974. https://doi.org/10.1175/JHM-D-13-0176.1

Kim, Y.-J., & Doyle, J. D. (2005). Extension of an orographic-drag parameterization scheme to incorporate orographic anisotropy and flow blocking. Quarterly Journal of the Royal Meteorological Society, 131, 1893–1921.

Lott, F., & Miller, M. J. (1997). A new subgrid-scale orographic drag parameterization: Its formulation and testing. Quarterly Journal of the Royal Meteorological Society, 123, 101–127.

458 Mcfarlane, N. A. (1987). The effect of orographically excited gravity-wave drag on the
459 general-circulation of the lower stratosphere and troposphere. Journal of the
460 Atmospheric Sciences, 44(14), 1775–1800.
461 https://doi.org/10.1175/1520-0469(1987)044<1775:Teooeg>2.0.Co;2

462 Nappo, C. J., & Chimonas, G. (1992). Wave exchange between the ground surface and a
463 boundary layer critical level. Journal of the Atmospheric Sciences, 49, 1075–1091.

464 Neiman, P. J., Schick, L. J., Ralph, F. M., Hughes, M., & Wick, G. A. (2011). Flooding in
465 western Washington: The connection to atmospheric rivers. Journal of
466 Hydrometeorology, 12(6), 1337–1358. https://doi.org/10.1175/2011JHM1358.1

467 Nuss, W. A., & Miller, D. K. (2001). Mesoscale predictability under various synoptic
468 regimes. Nonlinear Processes in Geophysics, 8, 429–438.https://doi.org/10.5194/npg-
469 8-429-2001

470 Picard, L., & Mass, C. (2017). The sensitivity of orographic precipitation to flow
471 direction: An idealized modeling approach. Journal of Hydrometeorology, 18, 1673–
472 1688. https://doi.org/10.1175/JHM-D-16-0209.1

473 Phillips, D. S. (1984). Analytical surface pressure and drag for linear hydrostatic flow
474 over three-dimensional elliptical mountains. Journal of the Atmospheric Sciences, 41,
475 1073–1084.

476 Rayner, N.A., P.Brohan, D.E.Parker, C.K.Folland, J.J.Kennedy, M.Vanicek, T.Ansell and
477 S.F.B.Tett (2006), Improved analyses of changes and uncertainties in sea surface
478 temperature measured in situ since the mid-nineteenth century: the HadSST2 data
479 set. Journal of Climate. 19(3) pp. 446-469.

480 Scinocca, J. F., & McFarlane, N. A. (2000). The parametrization of drag induced by

stratified flow over anisotropic orography. Quarterly Journal of the Royal Meteorological Society, 126, 2353–2393.

WellsH, Vosper SB, Ross AN, Brown AR,Webster S.Wind direction effects on orographic drag. Q J R Meteor Soc. (2008) 134:689–701. doi: 10.1002/qj.247

Xie, J., Zhang, M., Xie, Z., Liu, H., Chai, Z., He, J. X., & Zhang, H. (2020). An orographic-drag parametrization scheme including orographic anisotropy for all flow directions. Journal of Advances in Modeling Earth Systems, 12, e2019MS001921. https://doi.org/10.1029/2019MS001921

Zhang, H., Zhang, M., & Zeng, Q. (2013). Sensitivity of simulated climate to two atmospheric models: Interpretation of differences between dry models and moist models. Monthly Weather Review, 141, 1558–1576. https://doi.org/10.1175/MWR-D-11-00367.1

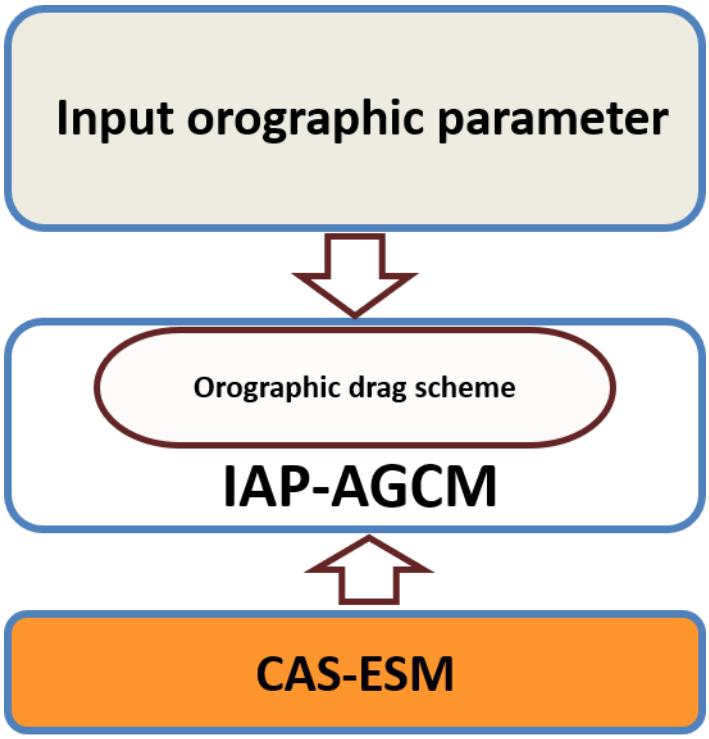

Fig. 1 Coupling of the orographic drag scheme with the CAS-ESM.

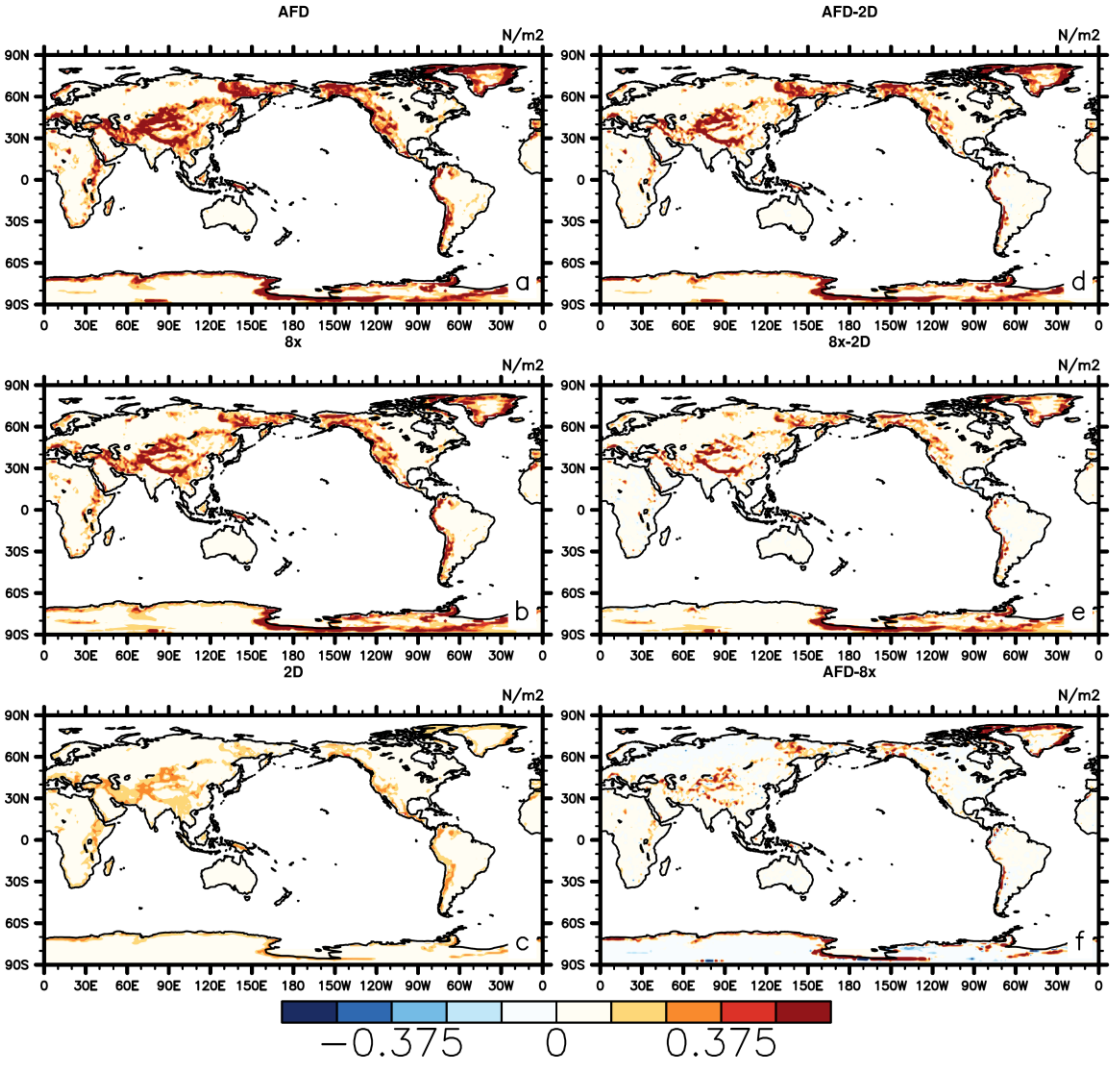

Fig. 2 Representative value (23 degree) for (a) AFD, (b)8x, (c) 2D, and representative difference (23 degree) of the surface drag (N/m2) for (d) AFD-2D, (e) 8x-2D, (f) AFD-8x.

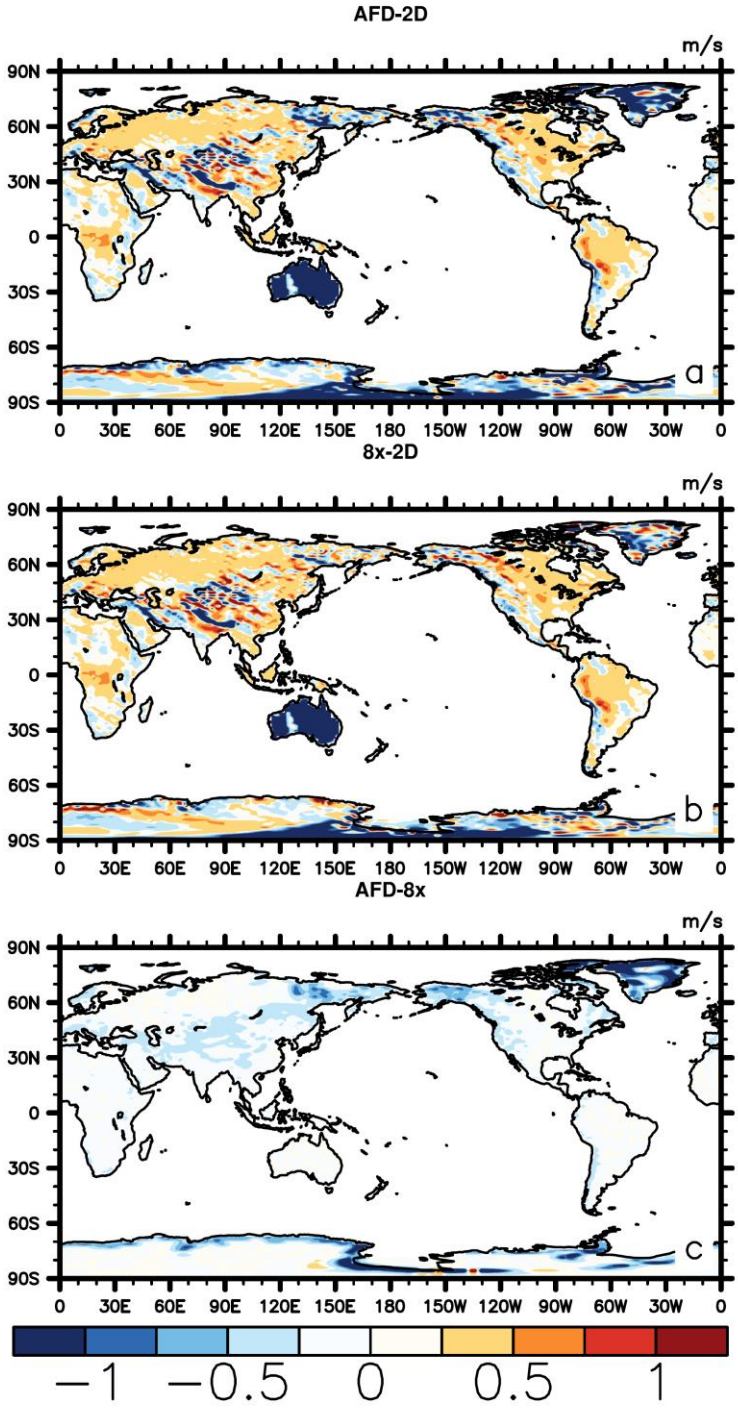

Fig. 3 Representative difference (23 degree) of the model bottom level (992-hPa) zonal and meridional wind (m/s) for (ab) AFD-2D, (cd) 8x-2D, (ef) AFD-8x.

505

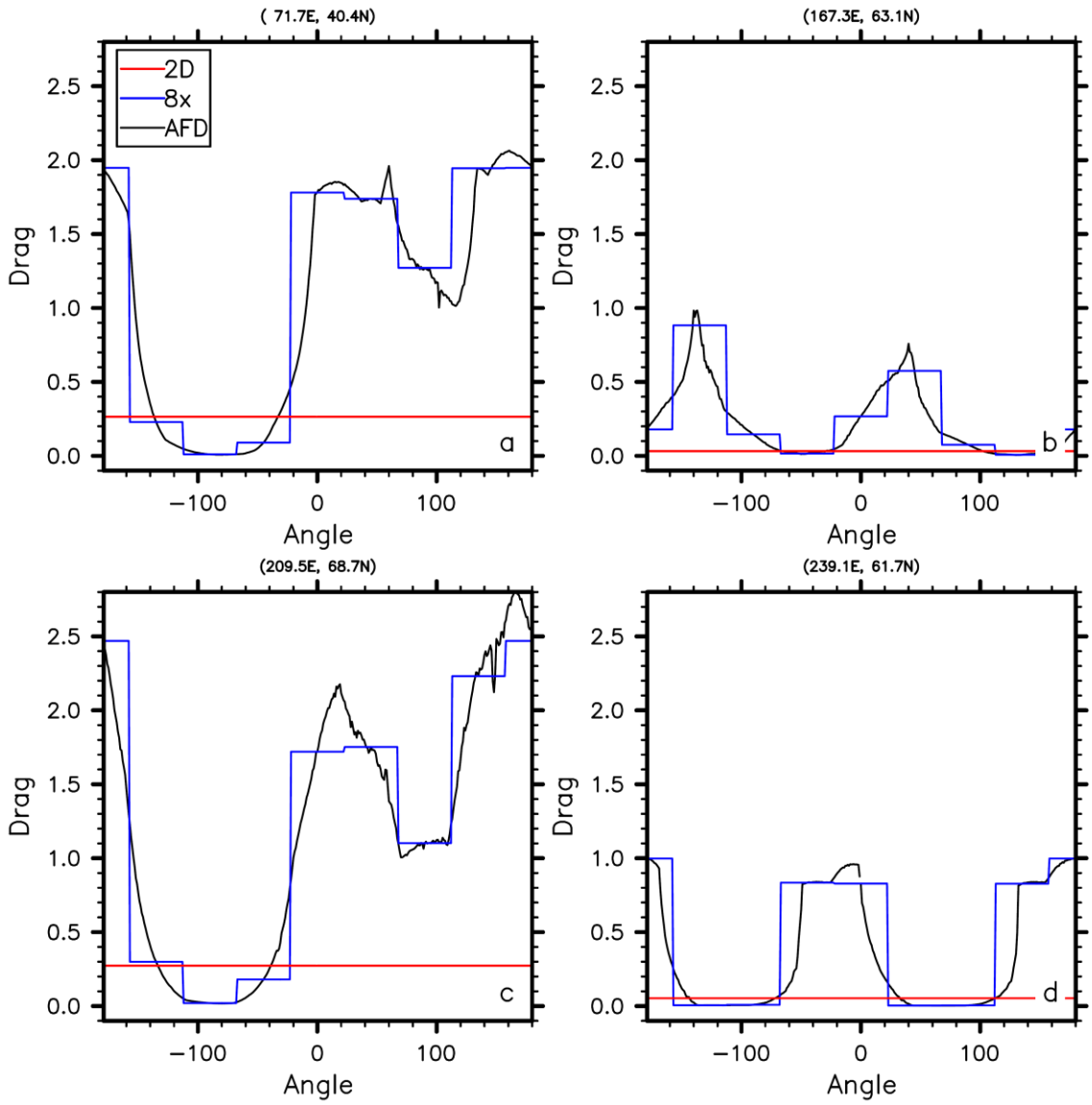

506

507 Fig. 4 Surface drag (N/m2) for the 3 schemes (AFD, 8x, and 2D) for the 4 points (a)
508 (71.7E, 40.4N), (b) 167.3E,63.1N, (c) (209.5E,68.7N), (d) (239.1E, 67.1N). The lines
509 correspond to AFD (black), 8x (blue), 2D (red).

510

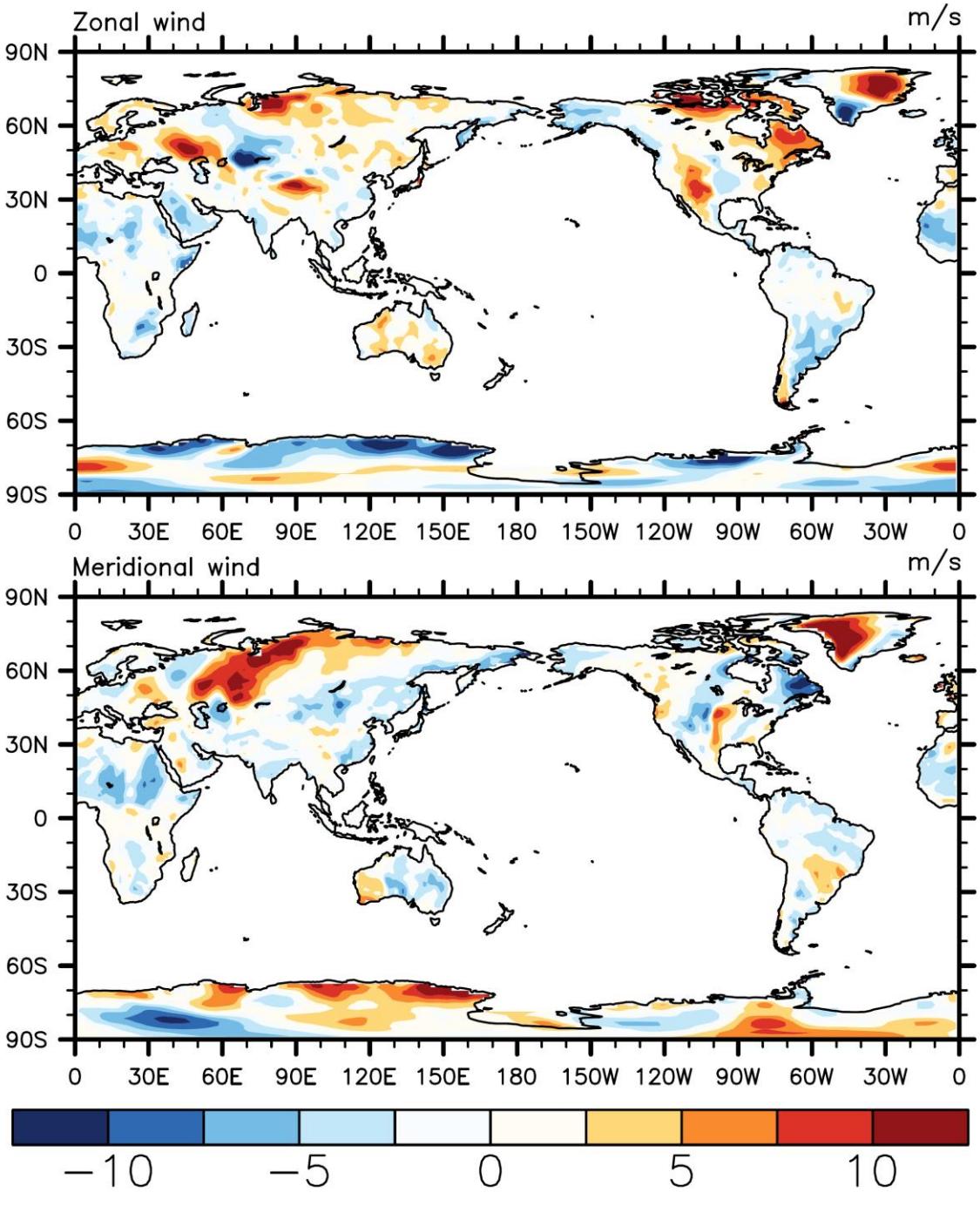

511

512 Fig. 5 The (a) zonal and (b) meridional bottom level wind for ECMWF initial condition
513 on 2016. Jan 21st.

514

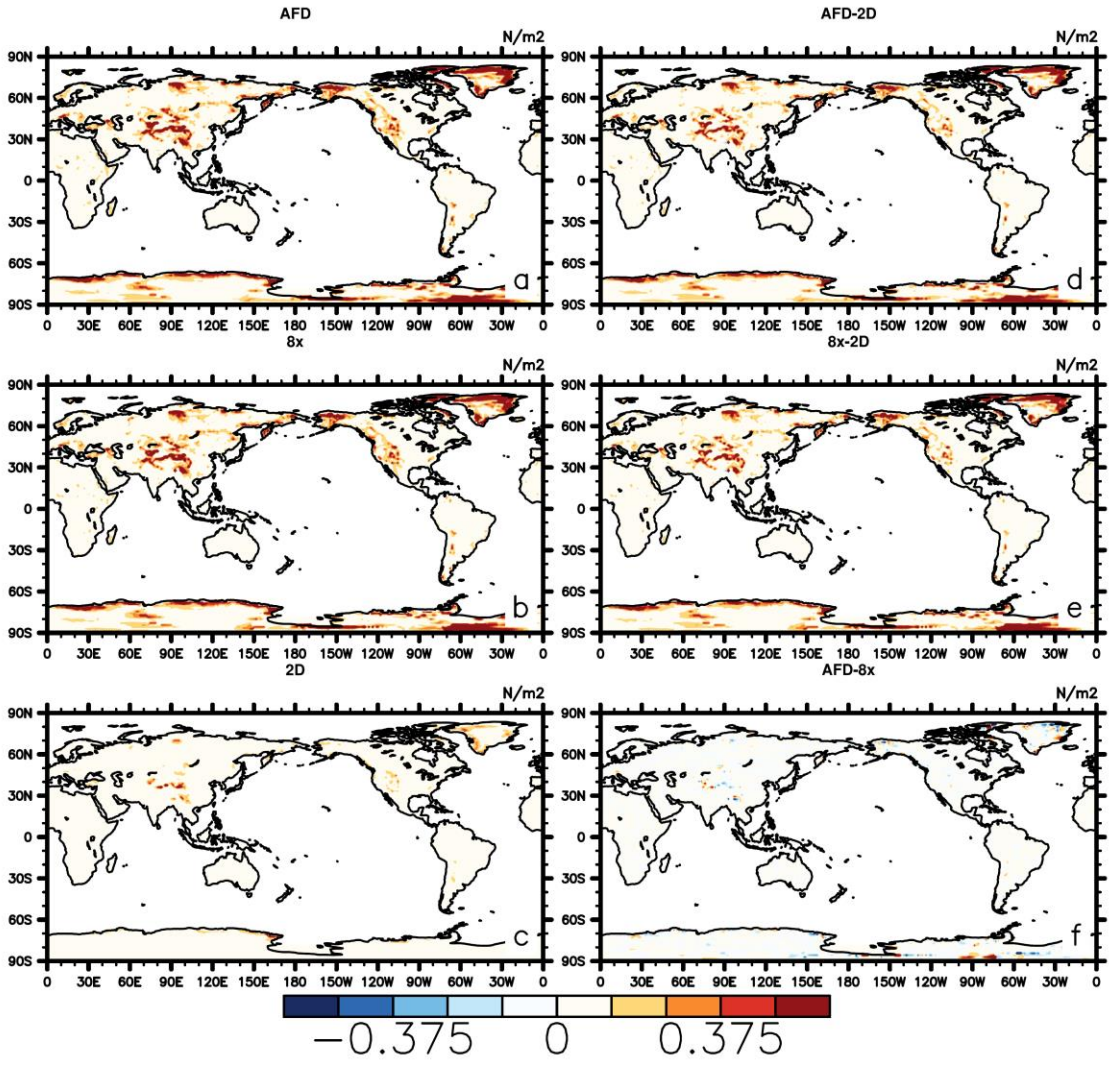

Fig. 6 Surface drag (N/m2) value for (a) AFD, (b)8x, (c) 2D, and the surface drag (N/m2) difference for (d) AFD-2D, (e) 8x-2D, (f) AFD-8x using ECMWF initial condition initialized on 2016.Jan 21st.

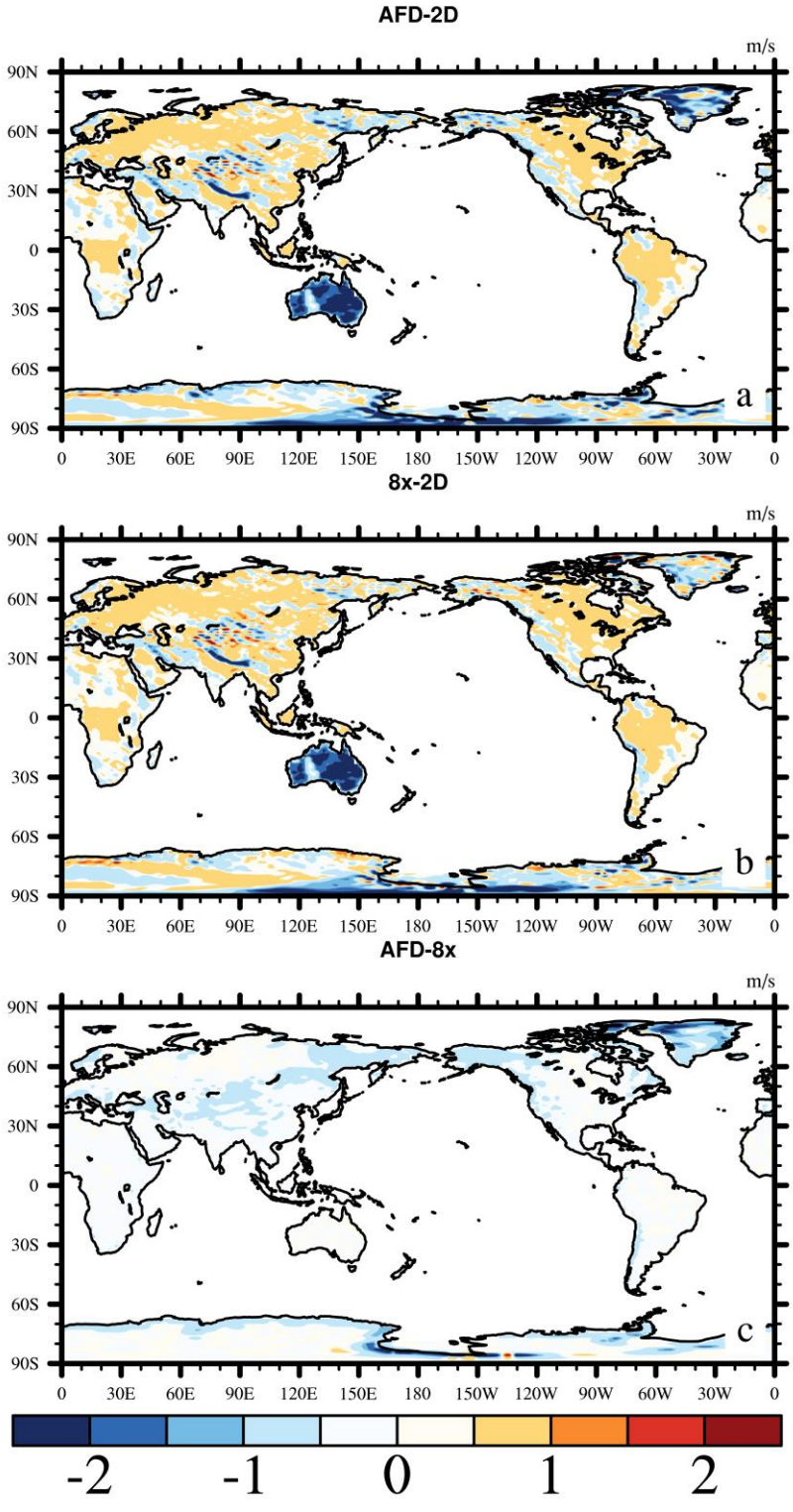
AFD-2D
m/s
90N
60N
30N
0
30S
60S
90S
0
30E
60E
90E
120E
150E
180
150W
120W
90W
60W
30W
0
a
8x-2D
m/s
b
AFD-8x
m/s
c
-2
-1
0
1
2

521

Fig. 7 Difference of the model bottom level (a) zonal and (b) meridional wind for AFD and 8x using ECMWF initial condition initialized on 2016. Jan 21st.

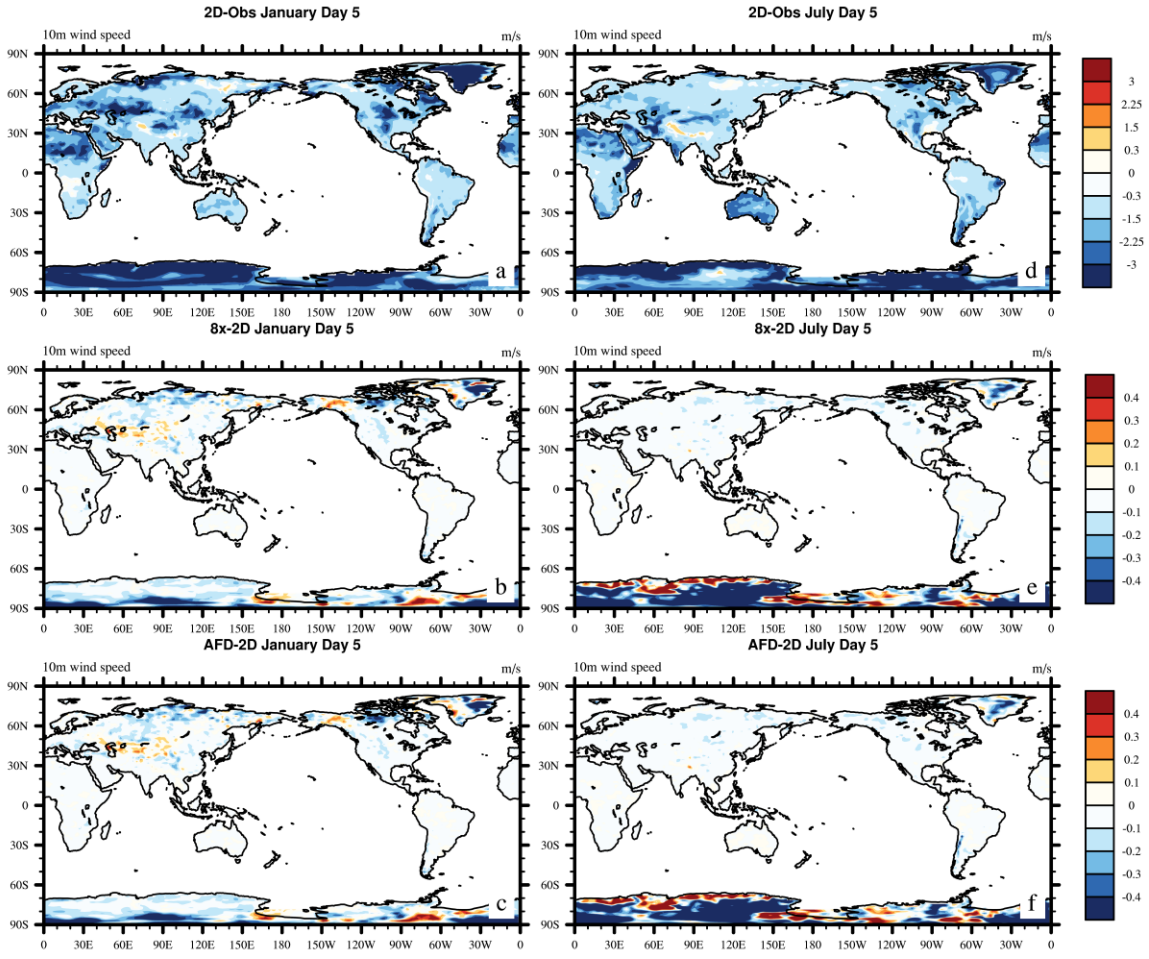

Fig. 8 Difference in 10-m wind speed (m/s) at forecast day 5 simulated by (ad) the 2-D scheme and the ERA-interim data, (be) 3D-8x scheme and 2-D scheme, (cf) 3D-AFD and 2-D scheme for January 2016 and for July 2016.

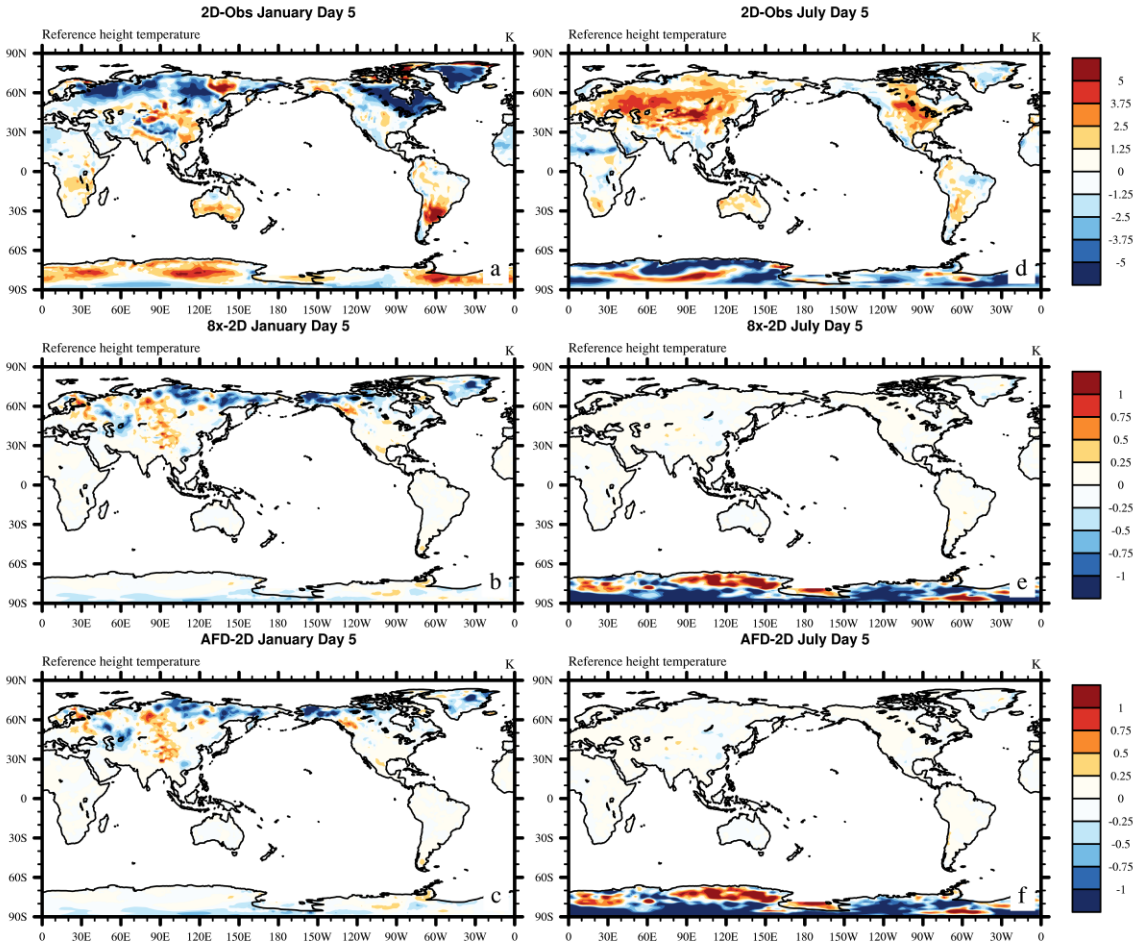

530

531 Fig. 9 Difference in surface drag (N/m2) at forecast day 5 simulated by (ac) 3D-8x
532 scheme and 2-D scheme, (bd) 3D-AFD and 2-D scheme for January 2016 and for July
533 2016.

534

535

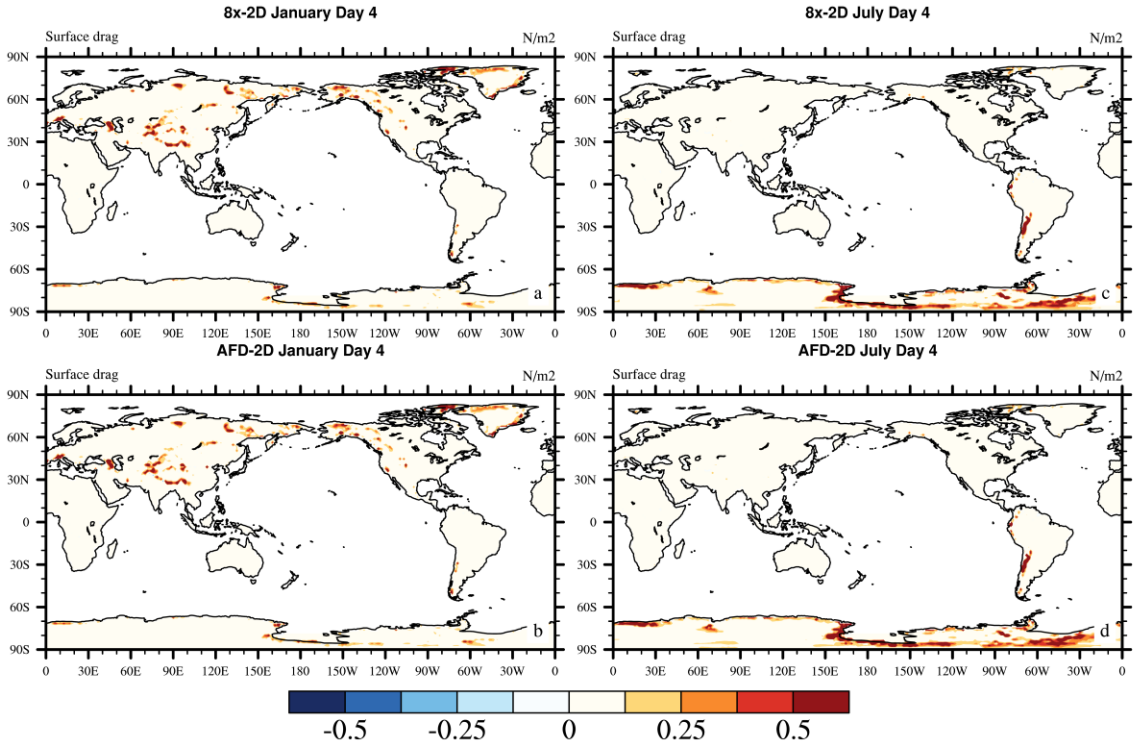

536

537 Fig. 10 Difference in surface drag (N/m2) at forecast day 5 simulated by (ac) 3D-8x
538 scheme and 2-D scheme, (bd) 3D-AFD and 2-D scheme for January 2016 and for July
539 2016.

540

541

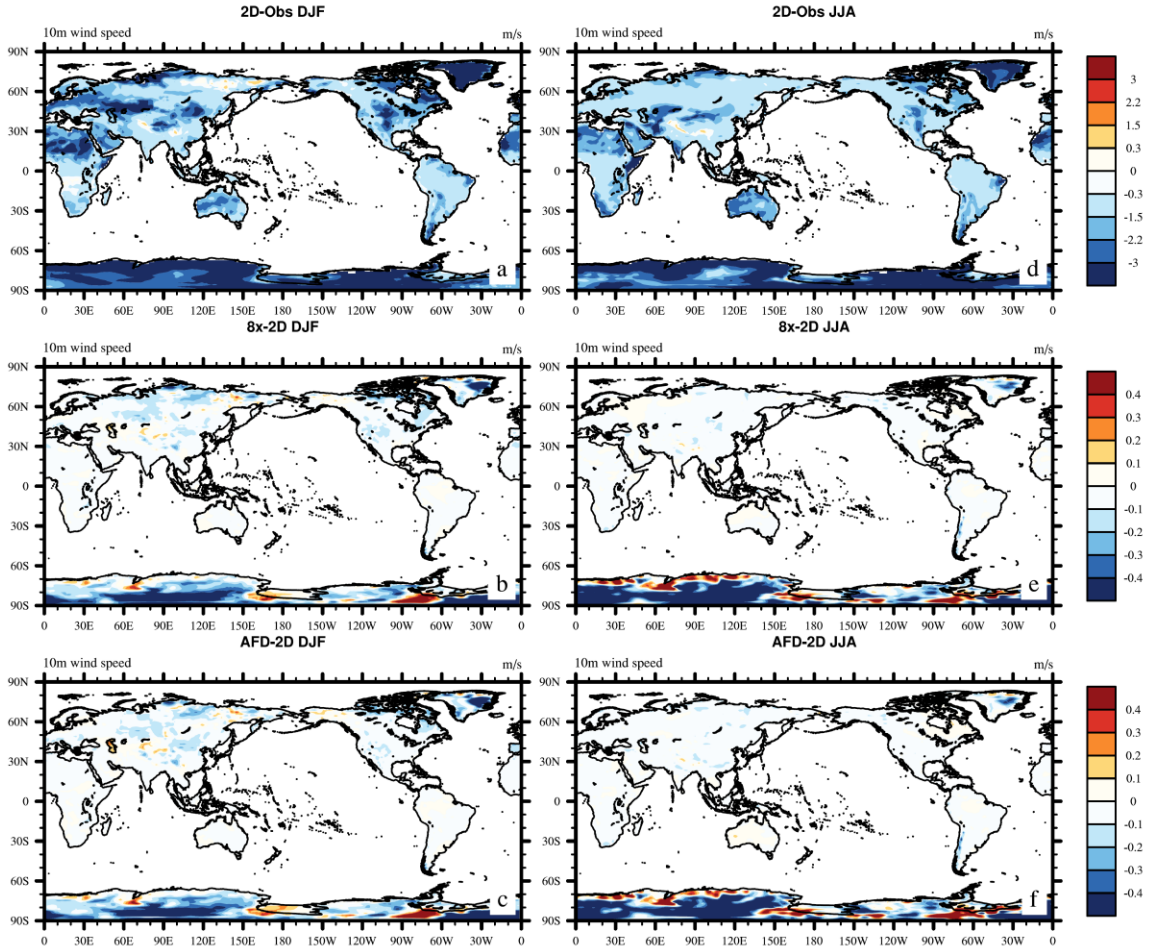

542

543 Fig. 11 Difference in DJF and JJA 10m wind speed simulated by (ad) the 2-D scheme and
544 the ERA-interim data, (be) 3D-8x scheme and 2-D scheme, (cf) 3D-AFD and 2-D
545 scheme for 2016.

546

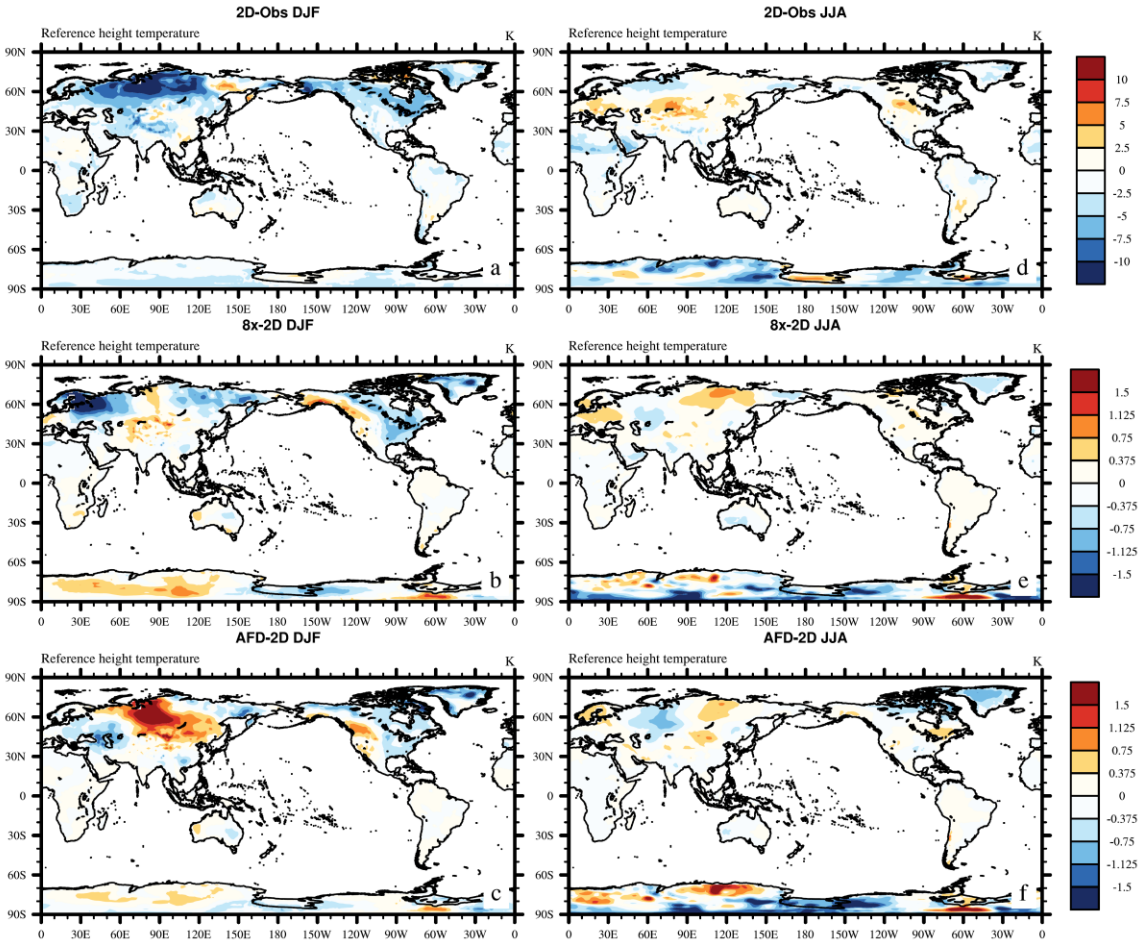

Fig. 12 Difference in DJF and JJA 10m wind speed simulated by (ad) the 2-D scheme and the ERA-interim data, (be) 3D-8x scheme and 2-D scheme, (cf) 3D-AFD and 2-D scheme for 2016.

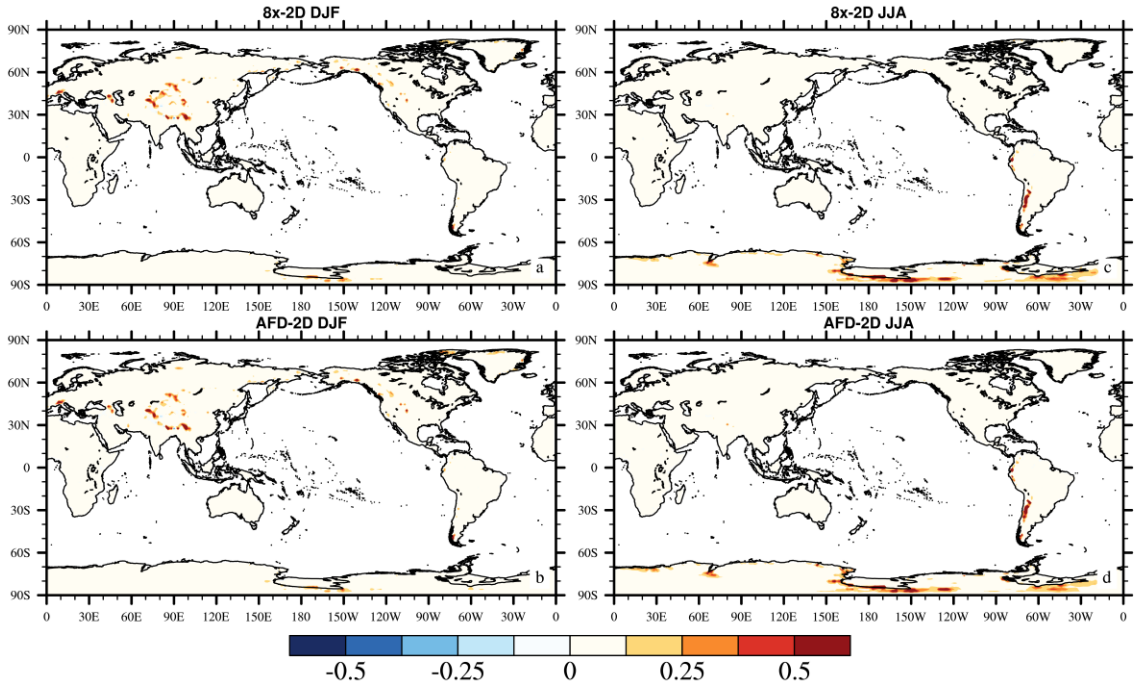

553

554 Fig. 13 Difference in DJF and JJA surface drag (N/m2) simulated by (ac) 3D-8x scheme
555 and 2-D scheme, (bd) 3D-AFD and 2-D scheme for 2016.

556

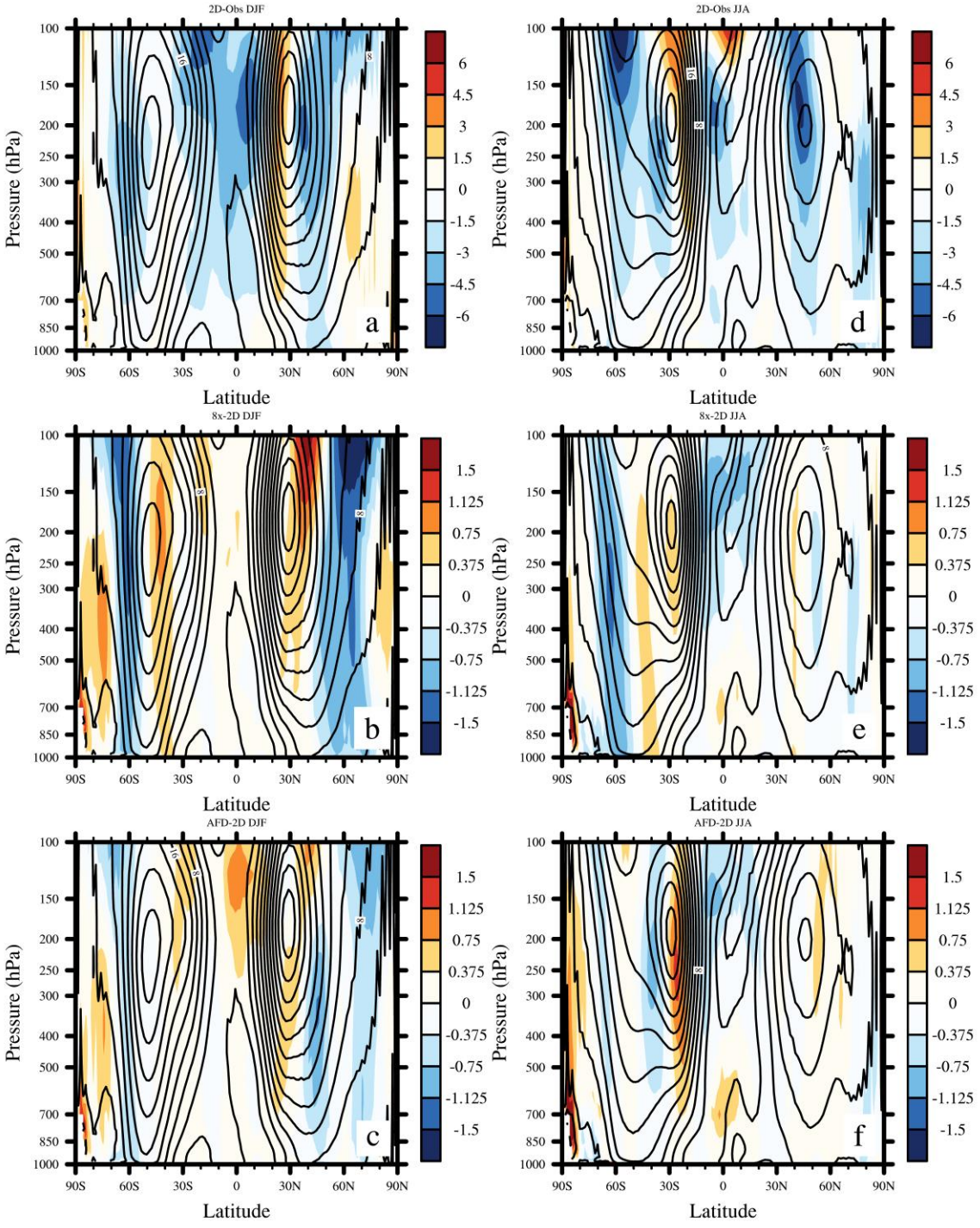

557

558 Fig. 14 Difference in global DJF and JJA zonal wind (m/s) simulated by (ad) 2-D scheme
559 minus observation, (be) 3D-8x minus 2-D, and (cf) 3D-AFD minus 2-D for 2016. The
560 contour denotes the 2-D zonal wind in DJF and JJA for (abc) and (def), respectively.

561

562